In situ quasi-elastic scattering characterization of particle size effects on the hydration of tricalcium silicate

A.J. Allen,[a] J.C. McLaughlin, and D.A. Neumann
Materials Science and Engineering Laboratory, National Institute of Standards and Technology, Gaithersburg, Maryland 20899

R.A. Livingston
Office of Infrastructure Research and Development, Federal Highway Administration, McLean, Virginia 22101

(Received 24 March 2004; accepted 26 July 2004)

The effects of different particle size distributions on the real-time hydration of tricalcium silicate cement paste were studied in situ by quasi-elastic neutron scattering. The changing state of water in the cement system was followed as a function both of cement hydration time and of temperature for different initial particle size distributions. It was found that the length of the initial, dormant, induction period, together with the kinetics of hydration product nucleation and growth, depends on the hydration temperature but not on the particle size distribution. However, initial particle size does affect the total amount of cement hydrated, with finer particle size producing more hydrated cement. Furthermore, the diffusion-limited rate of hydration at later hydration time is largely determined by the initial tricalcium silicate particle size distribution.

I. INTRODUCTION

Although Le Chetalier[1] discovered the basic process of Portland cement hydration over a century ago, many details of the cement hydration reaction kinetics remain uncertain. However, for the principal reaction responsible for setting and hardening Portland cement—between tricalcium silicate and water—it is generally recognized that it can be split into three steps.

First, after the end of an initial dormant induction period, tricalcium silicate dissolves in an irreversible exothermic reaction[2]

$$Ca_3SiO_5(s) + 3H_2O \rightarrow 3Ca^{2+}(aq) + 4OH^-(aq) + H_2SiO_4^{2-}(aq) \quad , \qquad (1)$$

where the third reaction product term represents a collection of silicate species. Second, when ion concentrations are sufficient, calcium-silicate-hydrate gel is precipitated from the solution through the reaction

$$H_2SiO_4^{2-}(aq) + xCa^{2+}(aq) + (2x - 2)OH^-(aq) + (y - x)H_2O(1) \rightarrow (CaO)_x(SiO_2)\cdot(H_2O)_y \quad . \qquad (2)$$

The CaO/SiO_2 ratio x varies with both hydration time and temperature, usually between one and two but always less than three.[2–4] Thus, excess Ca^{2+} ions result from this reaction.[5] Since the pore solution reaches saturation relatively rapidly, calcium hydroxide precipitates out in a third reaction

$$Ca^{2+}(aq) + 2OH^-(aq) \rightarrow Ca(OH)_2(s) \quad . \qquad (3)$$

Equations (1)–(3) can be combined to write a single (idealized) hydration reaction

$$Ca_3SiO_5 + (3 + y - x)H_2O \rightarrow (CaO)_x(SiO_2)(H_2O)_y + (3 - x)Ca(OH)_2 \quad , \qquad (4a)$$

or in cement notation[6]

$$C_3S + (3 + y - x)H \rightarrow C_xSH_y + (3 - x)CH \quad . \qquad (4b)$$

However, it should be noted that Eq. (1) is largely controlled by diffusion-limited (DL) kinetics while Eqs. (2) and (3) are controlled by nucleation and growth (NG) kinetics. This suggests that the overall hydration process might have a complex dependence both on the hydration conditions and on cement powder morphology. In this paper, we present a study of the effects of the particle size distribution on the hydration of tricalcium silicate C_3S.[6]

Kondo and Ueda[7] presented the first experimental data, derived from x-ray diffraction, for the hydration of monodispersed C_3S particles. In the same conference proceedings, Taplin[8] pointed out the need to consider the cement powder particle size distribution in models of cement hydration. Pommersheim et al.[9,10] attempted to

[a]Address all correspondence to this author.
e-mail: andrew.allen@nist.gov
DOI: 10.1557/JMR.2004.0415

parameterize the hydration process, including the induction period, in a model incorporating both an "accelerator" hydration regime and a later DL regime. However, most of the processes considered were effectively diffusion-limited. Knudsen[11] developed a theoretical hydration model for Portland cement that allows for dispersion in cement particle size. The hydration kinetics is divided into two distinct regimes governed by "linear" kinetics and by "parabolic" kinetics. The model was tested primarily against cement shrinkage[12] measurements made as a function of hydration time, and it was concluded that dispersion in cement particle size does indeed affect the shape of the hydration curve versus time. However, good agreement was not obtained for the early stages of hydration. Brown et al.[13] developed a hydration model for C_3S based on interface-process-controlled C–S–H formation until the end of the peak hydration period, and DL C–S–H formation thereafter. This approach has formed the basis of many subsequent models, but variability in the cement particle size distribution has remained an obstacle to applying such models in reliably predicting the cement property evolution during hydration.

In recent years, several approaches have been taken to address cement particle size variability in cement hydration studies. Bentz et al.[14,15] have incorporated the measured cement particle size distribution into a hydrating microstructure model that has been validated against cement shrinkage measurements[16] and which considers the largely DL consumption of cement particles in the hydration reactions. Parrott et al.[17] have compared the various "conventional" methods of measuring the degree of hydration: shrinkage, quantitative x-ray diffraction, nonevaporable water measurement, and conduction calorimetry. Broad agreement is found among these techniques with respect to variations in particle size distribution but not always with respect to compositional variation. The development of the C–S–H gel phase has also been followed as hydration proceeds, both by nuclear magnetic resonance[18,19] and by small-angle neutron scattering (SANS).[20–23] These studies have shown that the C–S–H gel development, together with associated changes in the cement morphology and pore water ion concentrations, should not be neglected if the hydration kinetics are to be understood.

Perhaps the most direct measure of the degree of cement hydration is that provided by quasi-elastic neutron scattering (QENS) studies.[24–26] In QENS the characteristics of the neutron recoil due to interactions with hydrogen (protons) are exploited to quantify the proportions of free water, surface-adsorbed water, and bound water of hydration present within a representative cement sample volume as a function of hydration time. QENS studies can explore in situ the undisturbed hydration reactions to determine the nature of the water in hydrating cement, or they can use the same information to explore the properties of the overall cement. Fratini et al.[27–29] have focused on the former (establishing a master curve for the development of "glassy" semi-bound water) while other authors have focused on the hydrating cement system, itself.[24–26,30–32]

QENS studies of hydrating cement permit quantitative analyses to be made both of the NG-controlled peak-reaction-rate hydration regime and of the subsequent DL-reaction hydration regime. However, separation of these two regimes can present challenges when there is a significant period of overlap. This is partly due to a nonintegral rate exponent encountered for the NG-controlled regime. Recently, Livingston[34] has pointed out that the nonintegral rate exponent may be associated with the fractal nature of the C–S–H gel hydration product.[20] Thomas and Jennings[35] have shown that conduction calorimetry can provide an accurate determination of the rate exponent, independently from QENS and have established that the exponent takes a constant value for a wide range of cement systems. In this paper, we build on this research to present in situ QENS studies that quantify the effects of cement particle size distribution on the hydration of C_3S. We also explore how the particle size distribution affects the DL reaction rate at later hydration times relative to the NG reaction rate at earlier times for hydration at three different temperatures: 20, 30, and 40 °C.

II. THEORETICAL MODEL FOR CEMENT HYDRATION

QENS measurements of hydrating cement systems[24–36] can distinguish three water components: free, fixed or completely-bound (CB), and pseudo-bound. Comparison of QENS and SANS[37,38] suggests that the pseudo-bound component is associated with water adsorbed on the surface of the solid hydration product, particularly the high surface area form of C–S–H gel. Experimentally, it is the sum of the CB and pseudo-bound component fractions that approximates to the "bound" water fraction. Here, we continue to define the bound water index (BWI) as the sum of the CB and pseudo-bound water fractions. However, we also consider the development during hydration of the CB water fraction, alone, since this is more closely associated (than is BWI) with the hydration reactions of Eqs. (1)–(4). Our hydration model is summarized below for the time dependence of BWI, but analogous equations can be written for the time dependence of CB.

Following FitzGerald et al.,[25] as amended by Thomas and Jennings,[35] it is assumed that cement hydration can be divided into the initial dormant induction period, a period of rapid hydration controlled by NG reaction kinetics and a subsequent slower hydration regime controlled by DL kinetics. We define a general hydration

time t, the hydration time after which the induction period ends t_i, and the hydration time after which DL reaction kinetics apply t_d. We also define the free water index (FWI) by FWI = 1 − BWI. It can be shown that the FWI time dependence in the NG regime is given by[25,35]

$$\mathrm{FWI}(t) = \mathrm{FWI}(t_i) - A_O[1 - \exp\{-[k(t - t_i)]^n\}] \quad , \tag{5}$$

where A_O is the BWI after infinite time in the absence of other diffusion-limited reaction, k is the NG reaction rate constant, and the exponent n is determined by the dimensionality of the system. Writing Eq. (5) in terms of BWI and assuming BWI(t) = 0 for all $t < t_i$ gives

$$\mathrm{BWI}(t)\big|_{t \geq t_i} = A_O\left[1 - \exp\left\{-\left[k\left(t - t_i\right)\right]^n\right\}\right] \quad , \tag{6}$$

and describes the increase of BWI with time during the NG regime. The reaction rate, d(BWI)/dt, peaks (below) with a maximum approximately proportional to the product, $\{nA_Ok\}$.

After hydration time t_d, it is assumed that the calcium and silicate ion concentrations in the pore water solution immediately available for C–S–H formation become exhausted, and the rate of increase of BWI(t) by NG kinetics becomes negligible compared with the DL rate of increase. The main diffusion process envisaged is that for water transport through C–S–H gel to reach the as-yet-unreacted cores of the original cement clinker particles. For a monodispersed population of cement clinker particles with an initial unreacted radius R a radius r after hydration time t and a water-to-cement mass ratio such that the free water is just consumed when the system is fully hydrated, FWI(t) is proportional to $(r/R)^3$. Following FitzGerald et al.,[30–32] it can be shown that at a hydration time $t > t_d$

$$[\mathrm{FWI}(t)]^{1/3} = [\mathrm{FWI}(t_d)]^{1/3} - R^{-1}(2D^*)^{1/2}(t - t_d)^{1/2} \quad , \tag{7}$$

where D* is an effective diffusion constant controlling water migration to sites where it can combine with unreacted cement.[33]

Whereas in previous work[30–32] the NG and DL regimes have been modeled separately, a single contiguous time-dependent hydration model is needed to quantify the effects of different initial particle size distributions on cement hydration over the full hydration time. For polydispersed initial cement particle sizes, the R^{-1} term in Eq. (7) must be averaged over the size distribution. On rewriting in terms of BWI and combining with the NG hydration regime described by Eq. (6), a full time-dependent model hydration curve can be obtained

$$\mathrm{BWI}(t) = \underset{t>0}{\mathrm{BWI}(0)} + A_O\left[1 - \exp\underset{(t_i \leq t \leq t_d)}{\left\{-\left[k\left(t - t_i\right)\right]^n\right\}}\right] + \left[1 - \left\{\left[1 - \mathrm{BWI}\left(t_d\right)\right]^{1/3} - \underset{(t > t_d)}{\left\langle R^{-1}\right\rangle}\left(2D_1^*\right)^{1/2}\left(t - t_d\right)^{1/2}\right\}^3\right] , \tag{8}$$

where D_1^* is an amended effective diffusion coefficient taking into account the particle size distribution, $\langle R^{-1}\rangle$ is the mean inverse radius averaged over the unhydrated cement clinker particle size distribution, and BWI(t_d) is the bound water index predicted by nucleation at time t_d. A nonzero bound water content BWI(0) is assumed even at zero hydration time to ensure that BWI(t) is everywhere positive. The model described by Eq. (8) explicitly assumes that only one of NG or DL kinetics is operative at a given hydration time. Such an assumption is necessary for fit convergence because of the total number of parameters required. While this implies a discontinuity, at least in the gradient of the fitted curve at $t = t_d$, no significant discontinuity is found for the higher hydration temperatures (30 and 40 °C), indicating that the two processes overlap for only a brief period. For hydration at 20 °C, a slight discontinuity is observed in some of the fitted hydration curves around time t_d, suggesting a more significant time overlap between the slower NG and DL regimes at this lower hydration temperature.

In principle, BWI(0), A_O, k, n, t_i, t_d, and D_1^* can be used as model fit parameters. However, the exponent n is more reliably evaluated from conduction calorimetry[35] than by QENS, and convergence is improved for the present fits with n held constant at 2.65. Good estimates for BWI(0) and t_i usually can be derived from the experimental QENS hydration curves. Furthermore, only a narrow range of t_d provides a smooth transition from NG to DL hydration kinetics. Thus, only A_O, k, and D_1^* are allowed to vary in the initial fitting, but final results are based on 6-parameter fits to the hydration curves. For a given C_3S particle size distribution and hydration temperature, the model can be applied separately to the BWI(t) and CB(t) hydration curves. To treat the CB water fraction, this can be used in place of BWI in Eq. (8).

From the Arrhenius temperature variations, activation energies can be derived for hydration based on either BWI or CB by assuming that the NG reaction rate constant k depends on the absolute temperature T and is given by

$$k(T) = k_O \exp\left\{-\frac{E_a}{R_m T}\right\}$$

and

$$\ln(k) = \ln(k_O) - \frac{E_a}{R_m T} \quad , \tag{9}$$

where E_a is the activation energy, R_m is the gas constant, and k_O is the rate constant in the limit of infinite temperature or zero E_a. Thus, a plot of $\{\ln(k)\}$ versus $\{-1/T\}$

offers a straight-line fit of gradient $\{+ E_a/R_m\}$. Finally, in the present analysis, two other hydration parameters are of interest. One is the hydration time t_{PK} at which the peak NG reaction rate (equal to $1.044A_O k$ for $n = 2.65$) occurs

$$t_{PK} = t_i + \left[\left(\frac{n-1}{n}\right)^{1/n}\right]\frac{1}{k} \quad . \tag{10}$$

The other is the ratio of the effective DL rate reaction constant effective at later hydration times to the NG reaction rate constant effective at early times.

This kinetic ratio is given by

$$\text{Kinetic Ratio} = \frac{\text{Diffusion}}{\text{Nucleation}} = \frac{2D_1^* \langle R^{-1}\rangle^2}{k} \quad . \tag{11}$$

While it might seem that the inverse of this ratio relates to the Thiele modulus discussed in the literature,[39] the Thiele modulus characterizes the relative importance of NG versus DL reaction processes occurring simultaneously within the same volume. Here, a DL reaction (mainly within unreacted cement particles) follows a NG reaction (mainly in the pore solution). This makes the (inverse) ratio of the DL to NG-controlled reaction constants the parameter of interest for comparing NG and DL reaction rates.

III. TRICALCIUM SILICATE POWDER PREPARATION AND SIZE ANALYSIS

The hydration experiments were performed on C_3S powder obtained from Construction Technology Laboratories (CTL, Skokie, IL). From the as-received C_3S, four chemically identical powders with different particle size distributions were prepared by grinding or milling for different times. Gross size distributions were confirmed by differential sieving, and the powders denoted as A, B, C, all ground with mortar and pestle, and D, puck-milled for 20 min.

Each anhydrous sample powder was suspended in ethanol and the C_3S particle size distribution measured by laser particle size analysis using a Beckman-Coulter LS-230 Particle Size Analyzer (Coulter Corporation, Miami, FL). The light source was a helium–neon laser with a wavelength of 632 nm. The Fraunhofer diffraction approximation[40] was used to determine the particle size distributions given in Fig. 1. For each sample, Fig. 1 presents the first differential of the integrated relative volume fraction of powder particles below a given diameter versus the sphere-equivalent particle diameter. While there is evidence in the size distributions for component sub-distributions that approximate to the shape expected for Weibull or Rossin–Rammler particle statistics,[41] it is clear that the overall distributions are more complex in nature. From the size distribution data, the mean particle diameter and the mean inverse particle radius $\langle R^{-1}\rangle$ can be deduced for use in Eqs. (7), (8), and (11). By sampling several independent particle size analyses for each C_3S sample, estimated standard deviations were computed which are presented with the mean values in Table I. For clarity one representative size distribution is presented for each sample (A, B, C, and D) in Fig. 1.

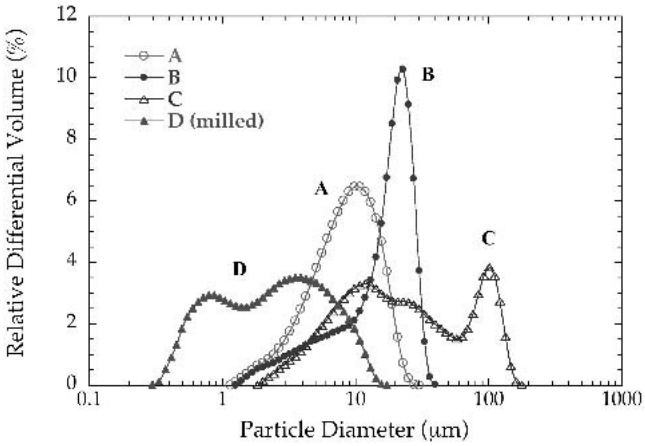

FIG. 1. Relative volume-weighted particle size distributions for the four C_3S samples, expressed as first-differentials of the integrated particle volumes smaller than a given diameter versus the sphere-equivalent particle diameter.

Repeated particle size analysis of equivalent powder batches provides a good means for determining the statistical uncertainties. It also aids rejection of erroneous results due to variable agglomerate or bubble formation in the ethanol suspensions. However, use of the Fraunhofer diffraction approximation is only strictly valid for particle diameters greater than about one micrometer. For finer sizes, either the full Mie scattering theory[42] is required or different approximations should be used (i.e., Rayleigh or Rayleigh–Gans scattering theory). Accurate knowledge of both the real and imaginary parts of the refractive index, not available here, is required for these corrections. As a result, particles smaller than 1 μm have been neglected for C_3S samples A, B, and C. For sample D, the milling results in a particle size distribution where submicrometer particles cannot be neglected. While use of the Fraunhofer diffraction approximation may lead to

TABLE I. C_3S particle size distribution parameters.

Sample	Volume-weighted mean particle diameter (μm)	Volume-weighted mean inverse radius (μm^{-1})
A	9.72 (58)	0.289 (18)
B	17.65 (16)	0.187 (17)
C	39.90 (40)	0.145 (10)
D (milled)	3.53 (10)	1.243 (38)

Numbers in parentheses are estimated standard deviations in least significant digits.

systematic uncertainty in the value of $\langle R^{-1} \rangle$ obtained, it is clear from Fig. 1 that sample D contains significantly finer particles than A, B, and C, thus justifying D's inclusion in the present study of particle size effects on hydration.

IV. IN SITU QENS ANALYSIS OF DEGREE OF HYDRATION

For the in situ QENS hydration studies, the C_3S was mixed at ambient temperature with de-ionized water to produce a cement paste with a 0.4 water-to-cement ratio by mass (0.4 w/c). After mixing by hand for 3 min, the paste was spread into a 0.5-mm-thick layer in an Al sample holder that was lined with Teflon to prevent the C_3S from reacting with the Al. By constraining the sample to this thickness (and a volume of area 40 × 60 mm), multiple scattering issues could be minimized in the QENS analysis. Finally, the sample holder was sealed using an indium gasket, thus ensuring that the total sample composition remained constant throughout the QENS measurements.

For each C_3S particle morphology separate QENS measurements were carried out using the NIST Fermi chopper time-of-flight (TOF) neutron spectrometer with samples maintained at set (continuously monitored) hydration temperatures of 20, 30, and 40 °C. QENS measurements commenced some 10 min after initial mixing, and the results were time-averaged in 30-min slices with data taken continuously for hydration times of up to 60 h, depending on the hydration temperature used.

QENS studies of C_3S hydration utilize three principles: (i) the scattering is dominated by that from the H atoms in the water and hydroxide groups present; (ii) the neutron can lose or gain energy in the neutron-proton interaction when the H (proton) is free to recoil; and (iii) the energy-transfer spectra for neutrons scattered by H in the free, pseudo-bound, and CB components are measurably different from each other. The overall energy-transfer spectrum is derived from measurement of the TOF distribution for scattered neutrons arriving at the instrument detectors after each Fermi chopper incident neutron pulse. Full details of the experimental configuration are given elsewhere.[31] With an incident neutron wavelength of 4.8 Å and sample-to-detector distance of 2.29 m, the calculated elastic scattering energy resolution ΔE is 0.146 meV.[43] The QENS energy-transfer spectrum obtained depends in general on the magnitude of the scattering vector Q for the elastic peak (no energy change) where $Q = (4\pi/\lambda)\sin(\Phi/2)$ and Φ is the scattering angle for a given instrument detector bank. To obtain sufficient statistics for accurate analysis of the energy spectrum, the data from several detector banks, corresponding to a range of Q, need to be summed together. Fortunately, at sufficiently high Q, the energy-transfer spectrum does not depend strongly on Q. For these studies, results were averaged over a Q range from 1.9 to 2.4 $Å^{-1}$.

In the case of cement hydration, it can be shown[32] that the QENS energy-transfer spectrum, $S(Q,\omega)$, where energy $= \hbar\omega$, $\hbar = h/2\pi$, and h is Planck's constant, can be modeled in terms of 4 components comprising a background term, an elastic peak delta function (zero energy transfer for CB H atoms), and two Lorentzian components for H atoms in the free and pseudo-bound water components

$$S(Q,\omega) = C_O + \left\{ P_O[\delta(\omega = 0)] + B_1\left[\frac{\Gamma_1}{\pi(\Gamma_1^2 + \omega^2)}\right] + B_2\left[\frac{\Gamma_2}{\pi(\Gamma_2^2 + \omega^2)}\right]\right\} \otimes \left(\frac{e^{-\omega^2/2\sigma^2}}{\sigma\sqrt{2\pi}}\right) \quad . \quad (12)$$

Here, C_O is a fixed intensity baseline (background), P_0 is the number density of CB H atoms, B_1 is the number density of free H atoms (in bulk water), Γ_1 is a Lorentzian half-width at half-maximum for the bulk water component, B_2 is the number density of H atoms in the form of constrained or pseudo-bound water, Γ_2 is a variable half-width-at-half-maximum fitting parameter, and σ is the Gaussian standard deviation of the measured resolution function of the spectrometer, which is convoluted with the three non-background components.

The QENS spectrum is analyzed over an energy-transfer range from −2 to +2 meV while C_O is determined from the flat data in the energy range at around −10 meV. The value of Γ_1 is determined from QENS measurements of pure water at the hydration temperature used.[31] In energy units, the full widths at half maximum ($2\hbar\Gamma_1$) for bulk water at 20, 30, and 40 °C are, respectively, 1.49, 1.87, and 2.23 meV. (The experimental standard deviations on these values are less than 0.16 meV.) Since σ is known from the instrument resolution function, this leaves only 4 free parameters for fitting Eq. (11) to each individual QENS spectrum: P_O, B_1, B_2, and Γ_2. In principle, for mean hydration time t, associated with a given 30-min QENS measurement, BWI(t) in Eq. (8) is given experimentally by the ratio $(P_O + B_2)/(P_O + B_1 + B_2)$, and the CB component CB(t), by the ratio $P_O/(P_O + B_1 + B_2)$. In practice, some elastic scattering occurs even at $t = 0$, and even the scattering from free water is not quite a pure Lorentzian.[27–29] Best results are obtained by measuring the changes in these ratios from their initial values at $t = 0$.[31] Thus, BWI(t) and CB(t) have been deduced from the changes with time in the associated ratios derived from a fit of Eq. (12) to the measured QENS spectrum.

V. RESULTS AND DISCUSSION

For the in situ QENS studies here, satisfactory hydration model fits were generally obtained using Eq. (8) for

both BWI(t) and CB(t). This supports our assumption of nucleation and growth without significant diffusion, followed by a DL hydration regime without significant NG. Only for some of the 20 °C curves do small discontinuities appear at the transition, suggesting a period of overlap between the NG and DL regimes. Furthermore, Eq. (2) is consistent with a NG regime description, also supported by SANS,[20–22] for C–S–H production occurring under high super-saturation conditions,[44,45] with ion concentration gradients in the pore solution both caused by and causing fluctuations in the reaction flux. In the subsequent DL regime, it is implicitly assumed that the gradients associated with nucleation and growth are no longer strong enough to overcome diffusion gradients that smooth out fluctuations in ion concentration, removing ions from locations where NG kinetics might otherwise continue.

Figure 2 presents typical variations of BWI(t) and CB(t) versus t at 30 °C for the four C_3S samples studied with model fits based on Eq. (8), or its equivalent for CB(t). Two observations can be made immediately. First, the finest C_3S particle distribution (sample D) gives significantly the largest amount of hydrated product, as measured by the greatest proportion of bound water development. Second, the statistical fluctuation of CB(t) is significantly less than that of BWI(t), despite BWI(t) being the larger quantity. This is because the elastic peak in the energy spectrum giving CB(t) is readily distinguishable from the two Lorentzian components whereas the two Lorentzians are not so easily distinguished from each other. This results in greater statistical overall uncertainty for BWI(t). Nevertheless, for all of the cases plotted in Fig. 2, excellent fits using the combined NG and DL model are obtained.

The QENS data obtained from actual hydration experiments can be compared with the predictions of theoretical models in the literature. For example, Fig. 3 presents the hydration curves predicted using the NIST CEMHYD3D[14,15] hydration model for the four samples with 0.4 w/c at 30 °C. This model is a cellular automaton-based code with lumped parameter kinetics yet distributed parameter phase definition. It is also based on shrinkage measurements and DL kinetics.[16] CEMHYD3D is of considerable engineering utility and many of the hydration characteristics predicted are qualitatively correct. However, the marked effect of fine C_3S particle size is underestimated, and other aspects of the hydration kinetics, as evidenced in the shape of the hydration curves in Fig. 2, are not fully captured. This underlines the need to include the process of cement hydration during the NG regime if a full understanding of the cement hydration kinetics is to be achieved.

Table II presents the fit results associated with BWI(t). Results are presented for the four different C_3S systems

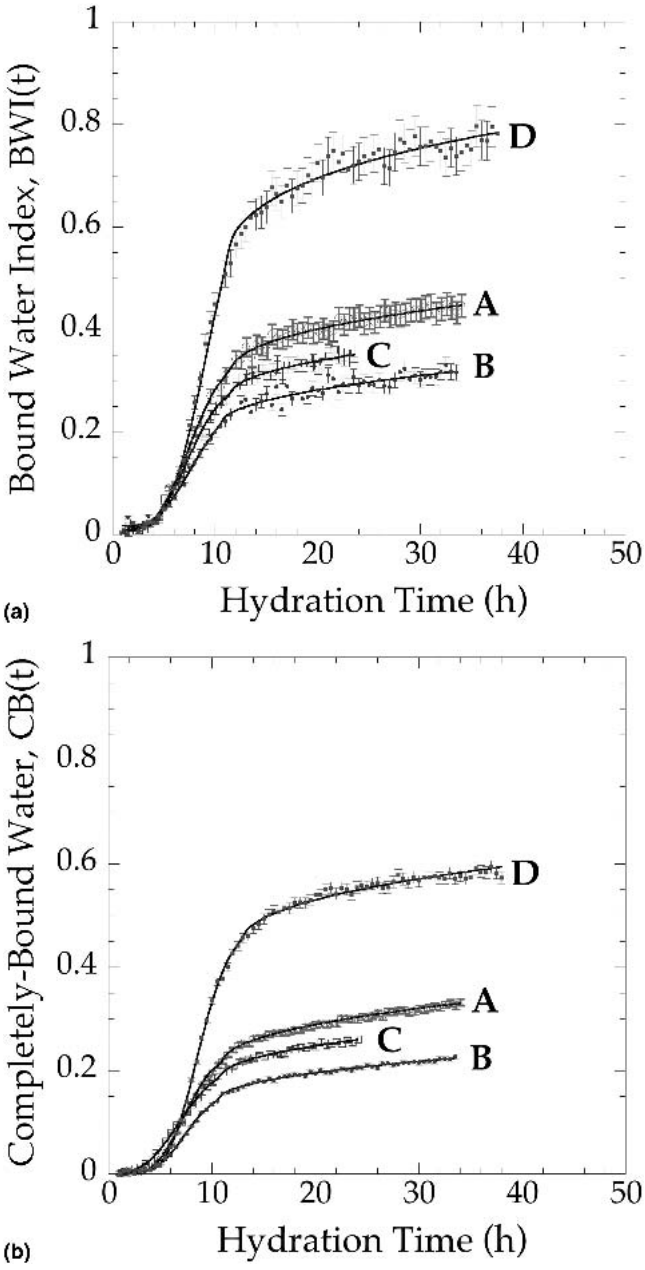

FIG. 2. (a) BWI(t) and (b) CB(t) versus hydration time for C_3S samples studied (0.4 w/c at 30 °C), together with model fits using the combined NG and DL hydration model of Eq. (8). Vertical bars are standard deviations derived from the QENS spectrum analysis using Eq. (12).

hydrated at the three different hydration temperatures. Where QENS studies were carried out on replicate samples, the QENS spectrum parameter values obtained by fitting Eq. (12) to the data sometimes show some variability, as observed for hydrating cement systems in general. Table II indicates how this variability affects the hydration parameters characteristic of the material chemistry, as given by Eq. (8). Table III presents the fit results associated with CB(t). The fit parameters obtained

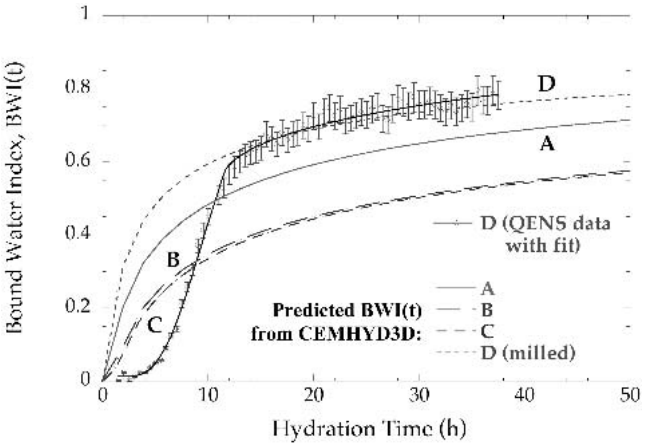

FIG. 3. Predicted hydration curves (0.4 w/c at 30 °C) using NIST CEMHYD3D[14,15] hydration model for the C_3S samples studied. The QENS data and fit for C_3S Sample D are also shown for comparison.

from CB(t) are close in value to those for BWI(t), except where further discussed below, and they follow the same general trends. This is not surprising because both components are determined by the same C_3S hydration kinetics. CB(t) represents all hydration reactions that consume free water, i.e., Eqs. (1)–(4), in which C–S–H and CH formation kinetics are superimposed on each other. BWI(t) includes the pseudo-bound component that is associated with the available surface area, which is dominated by the C–S–H gel relative to the coarse CH crystals. Thus, in the NG regime, BWI(t) is more heavily weighted in favor of C–S–H formation than is CB(t). However, a combination of previous SANS[20–22] and QENS[30–32] studies have shown that the pseudo-bound water is associated mainly with "outer-product" C–S–H formation between the C_3S particles, and may be absent from the subsequent dense "inner-product" C–S–H formation within the original boundaries of the un-hydrated C_3S particles. Particularly in the DL reaction regime, this means that BWI(t) is more heavily weighted towards outer-product formation than is CB(t). Given these different influences on the BWI and CB components, some differences in their time dependence are to be expected, especially at later hydration times.

The hydration reaction kinetics of C_3S hydration can be characterized by exploring the time-dependences of BWI(t) and CB(t) as a function both of hydration temperature T and of C_3S particle size. In this connection, it has been shown elsewhere[35] that the NG reaction rate exponent n is close to 2.65 for the hydration of a large range of cement systems. Here, a free fit of n, using Eq. (8) with the other parameters fixed, produces values between $n = 2.60$ and $n = 2.73$ over the entire range of C_3S samples and hydration temperatures studied. The value of 2.65 is close to the mass-fractal exponent found in SANS studies of the C–S–H outer-product microstructure.[46] For n fixed and the other parameters fitted in the NG regime, Tables II and III, and Fig. 4 indicate a modest reduction in A_O (less than 30% for the finest particles and smaller for coarser particles) with increasing T for both BWI and CB. However, there is a pronounced increase in A_O for fine C_3S mean particle size at all T. Since A_O is effectively a measure of the final C–S–H product volume resulting from NG processes, and SANS shows this hydration regime to be dominated by outer-product C–S–H formation,[20–22] these observations suggest that the final NG product volume is determined primarily by the surface area of the un-hydrated C_3S particles and the morphology of the available space between them. Fine C_3S particles lead to more uniform hydration (with some particles completely consumed) and a larger value of A_O. To a lesser extent, higher T gives more rapid but less uniform hydration, leading to a smaller overall value of A_O before hydration processes become diffusion-limited.

With reference to Eq. (12), it should be noted that, experimentally, the final values of BWI and CB under NG conditions are not given by their respective values of A_O, but are given by BWI(t_d) and CB(t_d). Measured as a fraction of A_O and as a function of either T or particle size, it might be assumed that BWI(t_d) and CB(t_d) would correlate with the relative prominence of the DL reaction kinetics at later hydration times. No such correlation was observed. Regardless of T or particle size, BWI(t_d) and CB(t_d) are found consistently to be 0.87 of the respective value of A_O, with an individual standard deviation of ±0.04. This lack of dependence may result from an insensitivity in the model fitting due to the large number of fit parameters that are significant around hydration time t_d, or it may arise from some other reason. However, this issue is not explored further here, and A_O is used to indicate the theoretical extent of the NG reaction kinetics.

For the NG reaction rate constant k, Tables II and III show that the main dependence is that of increasing k with T and no significant dependence on the C_3S particle size, except for a slight decrease with size at the highest hydration temperature 40 °C. The reaction constant k exhibits the expected Arrhenius variation with T for all of the C_3S systems studied, as is shown in Fig. 5 for sample D (milled). The activation energies E_a obtained on fitting Eq. (9) are given in Table IV. Calculations of E_a were carried out using both BWI(t) and CB(t) for each hydrating C_3S system. The values of E_a derived from the Arrhenius plots range between 30.4 and 44.4 kJ mol^{-1} K^{-1} with a mean of 37.1 ± 1.6 kJ mol^{-1} K^{-1}. This is consistent with recently reported values of E_a for the hydration of C_3S.[35] However, the variation of these derived values is somewhat greater than the computed standard deviations given in k. This is because of individual sample variability and also because the k-values, themselves, are obtained from the combined NG / DL hydration model

TABLE II. Fitted and derived hydration model parameters from BWI(t).

Sample	A_O	k (h^{-1})	D_1* (10^{-15} m^2 h^{-1})	t_i (h)	t_{PK} (h)	t_d (h)	$\{(2D_1^*) < R^{-1} >^2\}$ (10^{-5} h^{-1})	Kinetic ratio (10^{-5})
A								
20 °C (a)	0.332 (13)	0.097 (4)	1.1 (3)	4.2 (2)	12.8 (4)	17.3 (13)	18 (6)	183 (60)
20 °C (b)	0.338 (17)	0.076 (4)	1.3 (2)	3.2 (2)	14.2 (7)	18.9 (3)	22 (3)	292 (44)
30 °C (a)	0.336 (24)	0.144 (7)	0.9 (4)	1.5 (2)	7.3 (3)	11.7 (15)	15 (7)	101 (49)
30 °C (b)	0.367 (7)	0.125 (11)	1.0 (2)	2.6 (2)	9.3 (6)	11.3 (4)	16 (3)	126 (23)
40 °C (a)	0.270 (18)	0.206 (13)	0.6 (3)	2.2 (1)	6.3 (3)	8.9 (9)	10 (4)	46 (22)
40 °C (b)	0.271 (20)	0.217 (19)	0.9 (3)	1.4 (2)	5.3 (4)	7.6 (9)	15 (4)	67 (21)
B								
20 °C	0.207 (9)	0.086 (5)	1.1 (2)	5.8 (3)	15.5 (7)	20.3 (10)	7 (2)	86 (19)
30 °C (a)	0.246 (19)	0.132 (11)	1.1 (3)	1.4 (3)	7.8 (6)	10.5 (8)	8 (2)	58 (19)
30 °C (b)	0.177 (6)	0.253 (15)	1.8 (2)	4.2 (1)	7.5 (3)	10.0 (7)	12 (1)	49 (6)
40 °C	0.193 (10)	0.206 (15)	0.9 (1)	1.9 (2)	5.9 (4)	7.7 (3)	6 (1)	31 (4)
C								
20 °C	0.303 (12)	0.068 (3)	1.7 (6)	2.3 (4)	14.6 (7)	21.5 (15)	7 (2)	101 (36)
30 °C (a)	0.339 (30)	0.091 (6)	3.0 (6)	1.1 (3)	10.2 (7)	13.3 (17)	12 (2)	134 (28)
30 °C (b)	0.256 (6)	0.181 (10)	3.7 (6)	2.2 (1)	6.8 (3)	11.6 (10)	15 (2)	83 (14)
30 °C (c)	0.281 (13)	0.151 (10)	2.1 (9)	1.7 (2)	7.3 (4)	11.6 (10)	9 (5)	58 (31)
40 °C	0.256 (21)	0.175 (17)	2.6 (5)	1.4 (2)	6.1 (5)	10.3 (11)	11 (2)	61 (14)
D								
20 °C	0.673 (12)	0.071 (2)	0.10 (5)	6.8 (1)	18.6 (4)	24.5 (4)	32 (17)	454 (234)
30 °C (a)	0.612 (15)	0.127 (3)	0.05 (1)	4.1 (1)	10.7 (2)	14.4 (4)	16 (3)	123 (23)
30 °C (b)	0.742 (35)	0.122 (4)	0.34 (7)	2.4 (1)	9.2 (3)	11.3 (4)	105 (21)	865 (178)
40 °C	0.618 (14)	0.179 (3)	0.05 (1)	2.3 (1)	7.0 (1)	10.4 (4)	16 (4)	87 (22)

Numbers in parentheses are estimated standard deviations in least significant digits.

TABLE III. Fitted and derived combined hydration model parameters from CB(t).

Sample	A_O	k (h^{-1})	D_1* (10^{-15} m^2 h^{-1})	t_i (h)	t_{PK} (h)	t_d (h)	$\{(2\ D_1^*) < R^{-1} >^2\}$ (10^{-5} h^{-1})	Kinetic ratio (10^{-5})
A								
20 °C (a)	0.230 (3)	0.093 (2)	0.61 (4)	3.6 (1)	12.6 (3)	18.9 (1)	10 (1)	109 (7)
20 °C (b)	0.244 (5)	0.090 (2)	0.84 (4)	4.3 (1)	13.6 (3)	18.9 (1)	14 (1)	155 (8)
30 °C (a)	0.228 (3)	0.169 (4)	0.57 (4)	2.3 (1)	7.2 (2)	11.0 (1)	10 (1)	56 (4)
30 °C (b)	0.189 (3)	0.181 (2)	0.61 (15)	3.2 (1)	7.8 (1)	11.5 (2)	10 (3)	56 (14)
40 °C (a)	0.168 (3)	0.223 (6)	0.46 (8)	2.1 (1)	5.8 (1)	8.9 (5)	8 (1)	34 (6)
40 °C (b)	0.183 (3)	0.234 (5)	0.53 (4)	1.6 (1)	5.1 (1)	8.0 (2)	9 (1)	38 (3)
B								
20 °C	0.180 (2)	0.078 (2)	0.45 (4)	4.4 (2)	15.1 (3)	22.0 (2)	3 (1)	41 (4)
30 °C (a)	0.152 (3)	0.172 (5)	0.56 (8)	2.6 (1)	7.4 (2)	10.7 (4)	4 (1)	23 (3)
30 °C (b)	0.147 (2)	0.171 (4)	0.83 (4)	3.2 (1)	8.1 (1)	10.6 (1)	6 (1)	34 (2)
40 °C	0.160 (4)	0.188 (7)	0.53 (4)	1.6 (1)	6.0 (2)	8.0 (1)	4 (1)	20 (2)
C								
20 °C	0.323 (4)	0.067 (1)	1.24 (11)	2.9 (4)	15.4 (3)	20.0 (1)	5 (1)	77 (7)
30 °C (a)	0.178 (4)	0.078 (2)	1.10 (12)	4.4 (3)	15.1 (4)	19.9 (5)	5 (1)	59 (7)
30 °C (b)	0.205 (4)	0.135 (4)	1.60 (12)	1.1 (1)	7.3 (2)	11.0 (1)	7 (1)	49 (4)
30 °C (c)	0.202 (6)	0.138 (5)	1.41 (17)	0.8 (1)	6.8 (3)	10.9 (3)	6 (1)	42 (5)
40 °C	0.211 (4)	0.143 (4)	1.35 (9)	0.6 (1)	6.4 (2)	10.0 (2)	6 (1)	39 (3)
D								
20 °C	0.618 (9)	0.066 (1)	0.09 (1)	7.1 (1)	19.7 (3)	24.5 (4)	26 (4)	400 (60)
30 °C (a)	0.506 (9)	0.131 (2)	0.06 (1)	4.2 (1)	10.5 (1)	15.2 (4)	19 (3)	142 (22)
30 °C (b)	0.464 (4)	0.161 (2)	0.08 (1)	3.4 (1)	8.6 (1)	12.9 (3)	24 (3)	152 (18)
40 °C	0.491 (4)	0.196 (3)	0.03 (1)	2.7 (1)	7.0 (1)	9.8 (2)	9 (1)	45 (5)

Numbers in parentheses are estimated standard deviations in least significant digits.

described by Eq. (8), rather than by separate modeling of the two hydration regimes.

For C_3S sample D, Fig. 6 presents the variation versus T of the three previously defined hydration times, t_i, t_d, and t_{PK} for both BWI(t) and CB(t). Similar trends are found for samples A, B, and C. All three times decrease significantly with increasing T, but Tables II and III indicate little variation with the mean C_3S particle size

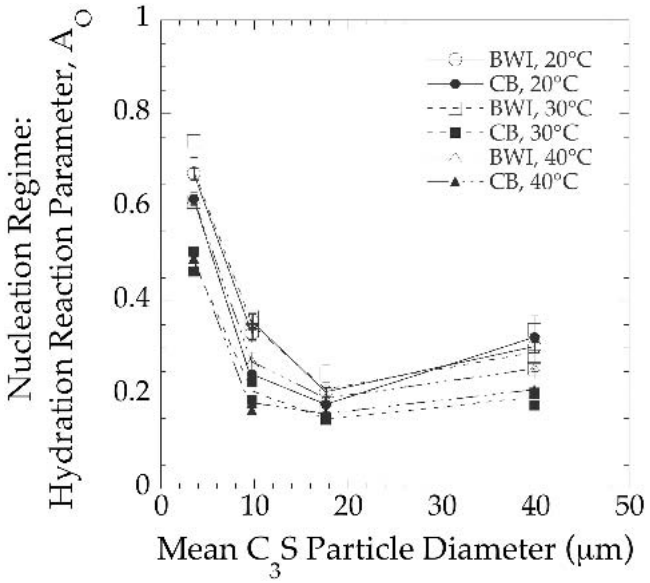

FIG. 4. Hydration reaction parameter A_O derived from fitting Eq. (8) to the measured BWI(t) and CB(t) versus un-hydrated mean C_3S particle diameter for all samples studied. Individual curves are plotted for BWI(t) and CB(t) at T = 20, 30, and 40 °C. Vertical bars are the computed standard deviations in A_O given by fits of Eq. (8).

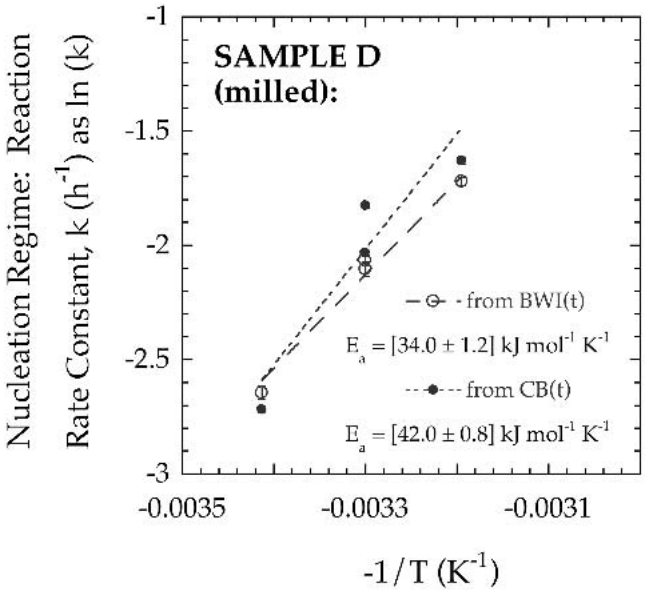

FIG. 5. Arrhenius plots of ln(k) versus {−1/T} determined from the BWI(t) and CB(t) NG hydration regime for C_3S system D (milled) using Eq. (9). Vertical bars are computed standard deviations in ln(k) derived from fits of Eq. (8).

(except for a slight decrease in t_i). Values obtained from BWI(t) and CB(t) are not significantly different, again indicating there is little difference in the dominant reaction kinetics underpinning BWI(t) and CB(t) in the NG regime. Indeed, a comparison of all the fit parameters that determine BWI(t) and CB(t) in the NG regime reveals a remarkable similarity between BWI(t) and CB(t)

TABLE IV. Activation energies for hydration during the NG regime.

C_3S system	A	B	C	D
E_a (kJ mol^{-1} K^{-1}) from BWI(t)	33.0 (22)	37.2 (35)	44.4 (33)	34.0 (12)
E_a (kJ mol^{-1} K^{-1}) from CB(t)	36.1 (9)	39.5 (16)	30.4 (11)	42.0 (8)

Numbers in parentheses are computed standard deviations in least significant digits from Arrhenius straight-line fits.

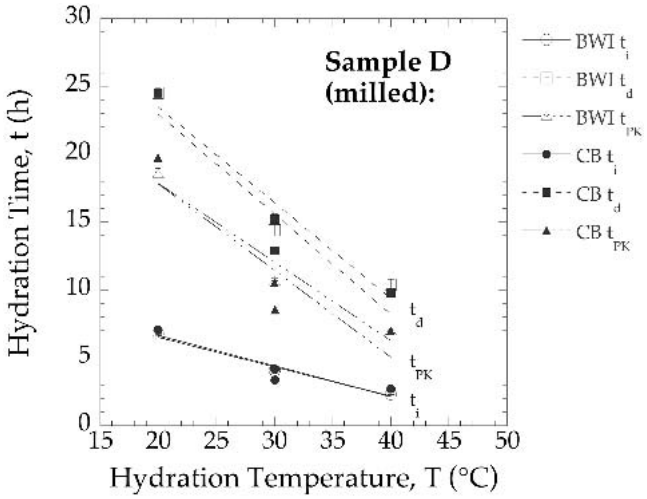

FIG. 6. Hydration times t_i, t_d, and t_{PK} versus hydration temperature T for C_3S sample D. Lines are guides to the eye. Vertical bars are computed standard deviations given by fits of Eq. (8), or derived from Eq. (10) in the case of t_{PK}.

for the entire range of samples and temperatures studied. With little or no correlation with C_3S particle size or T, the ratios of equivalent BWI(t) parameters to CB(t) parameters, together with their standard deviations (all derived from the data in Tables II and III), are given by: 1.39 ± 0.06 for A_O, 1.01 ± 0.05 for k, 1.11 ± 0.13 for t_i, 1.00 ± 0.02 for t_{PK}, and 0.97 ± 0.02 for t_d. This implies that only A_O is significantly different between BWI and CB. The difference is about 40% of the CB(t) component. Since BWI(t) differs from CB(t) only in that BWI(t) includes the surface-adsorbed water associated with C–S–H outer product, this is consistent with a NG regime dominated by outer-product formation. However, the subsequent formation of dense inner product C–S–H during the DL reaction regime causes some divergence between BWI(t) and CB(t) at later times.

Figure 7 presents the variation of the effective diffusion constant D_1* versus the mean C_3S particle size, derived from each of BWI(t) and CB(t) at each hydration temperature T. The value of D_1* can be associated with a representative average of the ion mobility within the pore solution and the water mobility through the C–S–H to access unhydrated C_3S. A significant increase in D_1*

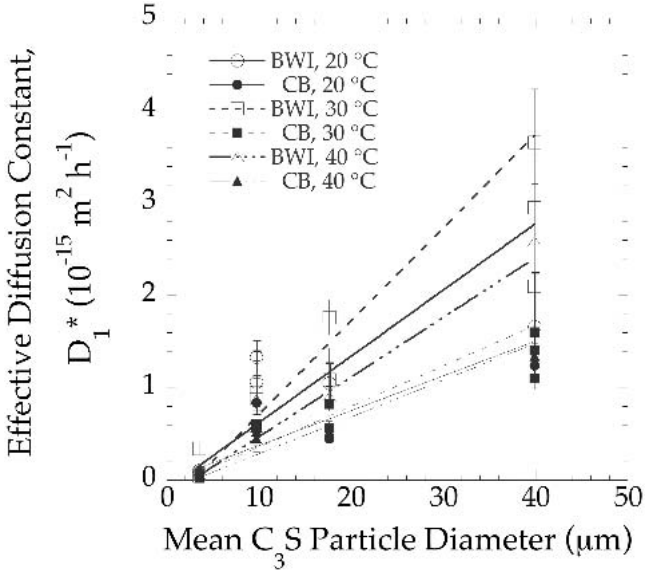

FIG. 7. Effective diffusion constant D_1* derived from fitting Eq. (8) to the measured BWI(t) and CB(t), versus un-hydrated C_3S mean particle diameter for all samples studied. Individual straight line fits are plotted for BWI(t) and CB(t) at T = 20, 30, and 40 °C. Vertical bars are computed standard deviations on D_1* given by the fits of Eq. (8).

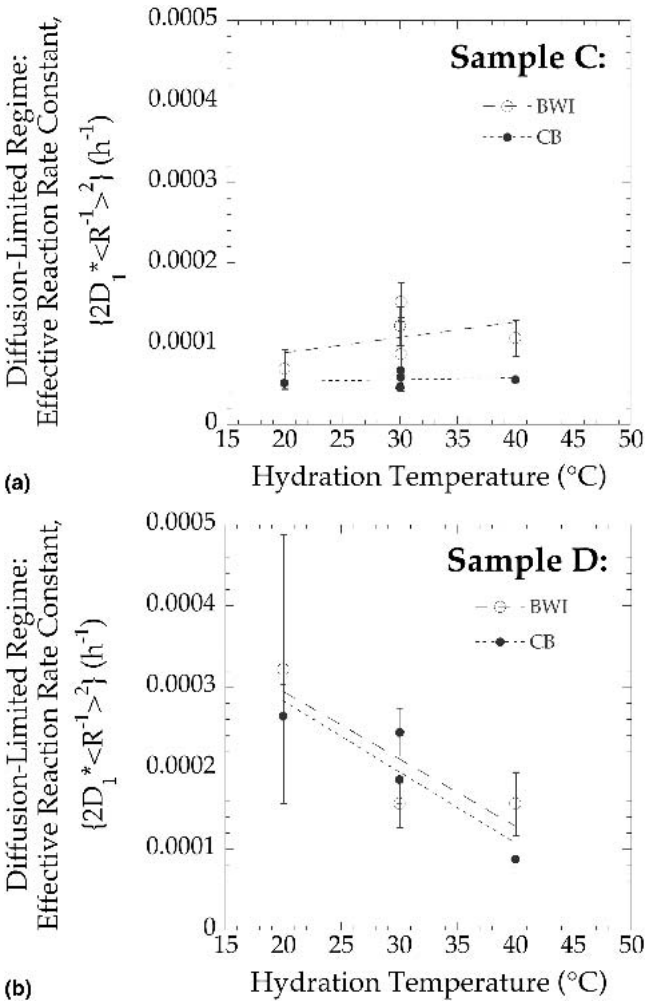

FIG. 8. Effective DL reaction rate constant, $\{2D_1^*\langle R^{-1}\rangle^2\}$ versus hydration temperature for (a) C_3S Sample C and (b) C_3S Sample D. Individual straight line fits are plotted for BWI(t) and CB(t). Vertical bars are the computed standard deviations given by the fits of Eq. (8).

occurs with increasing particle diameter at all T. Large inter-particle pores associated with coarse C_3S particles, together with reduced hydration product formation A_O in the NG regime, offer reduced impedance to the ion mobility in the DL regime, and this results in the increased D_1*. Tables II and III indicate that D_1* is not significantly T-dependent for coarse particle size but some decrease occurs with T for fine particles. This is consistent with earlier studies,[32] suggesting more rapid nucleation at higher T produces a microstructure that more greatly impedes later diffusion-driven transport, particularly for a fine pore/particle morphology. In all cases, D_1* is larger for BWI(t) than it is for CB(t), and the particle size dependence is also stronger for BWI(t).

The diffusion constant, D_1*, is not itself a measure of the DL hydration rate but the term, $\{2D_1^*\langle R^{-1}\rangle^2\}$, is an effective DL reaction rate constant, analogous to k for the NG hydration regime. (The exponents n or 1/2 must be taken into account to obtain the actual NG or DL reaction rates, respectively.) Using this definition, Fig. 8 shows that (following the trend for D_1*) the effective diffusion rate constant is not significantly T-dependent for coarse C_3S particles [Fig. 8(a)], but it decreases with T for fine particles [Fig. 8(b)]. However, the C_3S particle morphology (represented by the $\langle R^{-1}\rangle^2$ factor) does affect the rate constant dependence on particle size. Tables II and III show a significantly-increased DL reaction rate constant for the finest C_3S particles hydrating at 20 °C, but only a slight increase for fine particles hydrating at 30 or 40 °C. This is a different variation with C_3S particle size than found for D_1*, and is reflected in the corresponding variations, shown in Fig. 9, for the kinetic ratio of the DL/NG reaction constants defined by Eq. (11). Tables II and III indicate that the T dependence of the kinetic ratio is significantly stronger than for D_1* or for the DL reaction rate constant, but this is due mainly to the T dependence of the NG reaction constant k, discussed previously. The major result here is that of Fig. 9, which clearly associates enhanced DL C–S–H formation with fine C_3S particle size, particle size having already enhanced C–S–H formation by nucleation (where, recall, the peak NG reaction rate = $1.044kA_O$). Fine particles enhance the DL reaction rate because the diffusion distance over which water must migrate from the surface to reach un-hydrated material is significantly less than for coarse particles. It appears that this geometric effect more than compensates for the increased impedance of the fine morphology for the particle size dependence of D_1*.

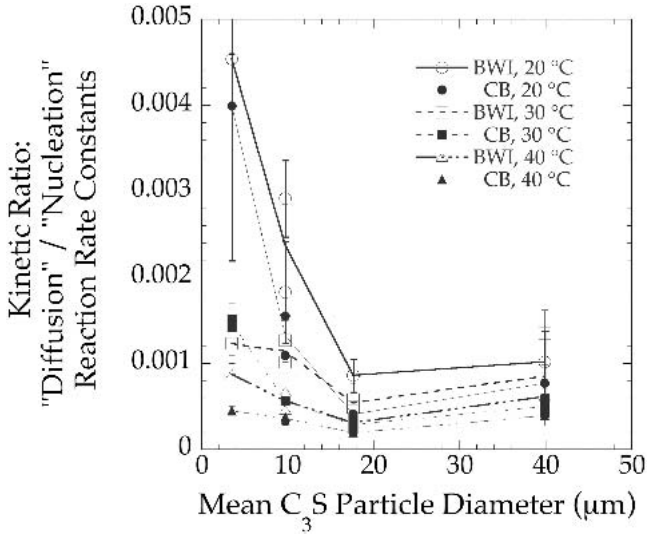

FIG. 9. Kinetic ratio of effective DL reaction rate constant to effective NG reaction rate constant versus un-hydrated C_3S mean particle diameter for all samples studied. Lines are guides to the eye. Vertical bars are the computed standard deviations given by the fits of Eq. (8).

The above discussion should be related to the previous literature on the effects of particle size on the hydration reactions in the DL hydration regime.[7–17] The Kondo model[7] uses a particle of fixed radius with a shrinking core of unreacted C_3S and a corresponding growing shell of C_3S. Pommersheim et al.[9,10] add a layer of deposited C–S–H so that the overall radius increases. The Knudsen model[11,12] concerns only the shrinking unreacted C_3S. It is not clear from the present results whether overall C_3S particle size increases, decreases, or remains constant during hydration. The unreacted composite C_3S particle cores must shrink as water diffuses into the particles, and the different behaviors for coarse [Fig. 8(a)] and fine [Fig. 8(b)] particles may indicate the ultimate dissolution of fine particles, though not coarse particles, in the DL regime. With the SANS results that show outer product C–S–H between cement particles to have a morphology quite separate from that of the particles themselves,[20–22] this could be taken as supportive of the Kondo model for cement hydration.[7]

Having made the distinction between BWI(t) and CB(t), their comparison in the two time regimes allows one to infer differences in the C–S–H morphology produced. The ratios of equivalent BWI(t) parameters to CB(t) parameters, together with their standard deviations, are given by: 1.86 ± 0.17 for both D_1* and the effective DL reaction constant, $\{2D_1^*\langle R^{-1}\rangle\}^{23}$, and 1.91 ± 0.23 for the kinetic ratio defined in Eq. (11). At an arbitrarily long hydration time $t = 2t_d$, Eq. (8) indicates the ratio of the actual DL increments in the BWI and CB components (compared to their NG values at $t = t_d$) is 1.21 ± 0.05. The reduction from the value of 1.39 ± 0.06 for the ratio of BWI to CB formation in the NG regime (see above) is strongly indicative of a different C–S–H morphology developing from the hydration reactions in the DL regime. At least some of the C–S–H contains significantly less pseudo-bound water, compared to the earlier NG-controlled outer-product C–S–H formation.

VI. SUMMARY AND CONCLUSIONS

Several important conclusions can be drawn from these in situ QENS studies of real-time C_3S hydration. C_3S particle size, not temperature, controls the size of the NG reaction volume; with fine C_3S particles giving a larger reaction volume (large A_O). Hydration temperature T, not particle size, controls the NG reaction rate constant, k, which increases with T, and the hydration time parameters, which decrease with T. The latter include the onset time for the DL regime. Nevertheless, fine C_3S particle size appears to increase the induction time t_i. If it is assumed that the induction period ends once significant hydration is apparent, then only a limited number of coarse particles need to commence hydration early to realize this condition. Conversely, a large number of fine particles must commence hydration early before the same condition is met, since far less material is available for hydration within each particle. Thus, a somewhat longer induction period is observed before significant hydration is apparent for finer particles.

The close relationship between BWI(t) and CB(t) throughout the NG regime strongly suggests that BWI(t) and CB(t) are associated with nucleation and growth of the same product structure. The only significant difference is that BWI(t) includes 40% more water than does CB(t). The additional water is in a pseudo-bound state and presumably is adsorbed on the surface of the C–S–H outer-product structure.[20–22]

In the DL hydration regime, the effective DL constant increases with increasing C_3S particle size for both BWI(t) and CB(t), with BWI(t) having both the stronger size dependence and larger absolute value for D_1*. However, due to the different particle morphology, the effective DL hydration reaction rate constant decreases with increasing C_3S particle size particularly for hydration at 20 °C, less so for hydration at 30 and 40 °C. These effects are consistent with greater diffusion-limited water and ion mobility for large C_3S particles where there is less C–S–H formation during the NG regime, but greater DL hydration for small particles due to the short diffusion distances associated with the fine particle size. The decrease with increased hydration temperature in both the diffusion constant and the DL reaction rate constant for fine particles can be attributed to more rapid NG at higher T producing a microstructure that more effectively impedes later diffusion-driven transport.

Also in the DL hydration regime, the fit parameters for BWI(t) and CB(t), over the entire range of samples and

temperatures studied, reveal a reasonably constant relationship between BWI(t) and CB(t). However, this relationship is different from that found in the NG regime, as may be quantified by use of the fit parameters in Eq. (8). With reference to our earlier discussion, the roughly constant ratios across the range of C_3S systems and hydration temperatures studied suggest that similar proportions of water may be associated with inner-product C–S–H, outer-product C–S–H and CH formation as the DL hydration regime progresses.

Perhaps the most important conclusions to be drawn from these studies are that fine C_3S particle size gives the most C–S–H formation for a given water-to-solids mass ratio, and that some aspects of the cement hydration kinetics exhibit behavior that may be universal in nature and related to fractal aspects of the microstructures formed. It will be of interest to determine in future studies to what extent these effects are applicable for w/c ratios other than 0.4, and to other cement systems such as C_2S and C_3S/C_2S mixes and to ordinary Portland cement.

ACKNOWLEDGMENTS

We acknowledge Dennis Minor of the National Institute of Standards and Technology, Gaithersburg, MD, for assistance with the laser particle size distribution analysis, and Jeffrey Thomas of Northwestern University, Evanston, IL, for invaluable discussions concerning the kinetics of cement hydration in general, and the NG-controlled regime in particular.

Information on commercial products is given for completeness and does not constitute or imply their endorsement by the National Institute of Standards and Technology.

REFERENCES

1. H.L. Le Chatelier: In *Experimental Researches on the Constitution of Hydraulic Mortars* (McGraw Publishing Co., New York, 1905).
2. J. Skalny and I. Odler: Effect of heat treatment on the pore structure and drying shrinkage behavior of hydrated cement paste. *J. Colloid Interface Sci.* **40,** 199 (1972).
3. I. Odler and H. Dorr: Tricalcium silicate formation by solid-state reactions. *Am. Ceram. Soc. Bull.* **56,** 1086 (1977).
4. A. Bentur, R.L. Berger, J.H. Kung, N.B. Milestone, and J.F. Young: Structural-properties of calcium silicate pastes 2. Effect of curing temperature. *J. Am. Ceram. Soc.* **62,** 362 (1979).
5. H.F.W. Taylor: In *Cement Chemistry* (Academic Press, London, U.K., 1990), pp. 153–156.
6. Cement chemistry notation: C = CaO, S = SiO_2, H = H_2O. http://www.wordiq.com/definition/cementchemistnotation.
7. R. Kondo and S. Ueda: Kinetics of Hydration of Cements, in *Proc. 5th Int. Symposium on the Chemistry of Cement. Vol. II.* (Cement Association of Japan Tokyo, Japan, 1969), p. 203.
8. J.H. Taplin: On the Hydration Kinetics of Hydraulic Cements, in *Proc. 5th Int. Symposium on the Chemistry of Cement. Vol. II.* (Cement Association of Japan Tokyo, Japan, 1969), p. 337.
9. J.M. Pommersheim, J.R. Clifton, and G.J. Frohnsdorff: Mathematical-modeling of tricalcium silicate hydration 2. Hydration sub-models and the effect of model parameters. *Cem. Concr. Res.* **12,** 765 (1982).
10. J.M. Pommersheim: Effect of particle size distribution on hydration kinetics, in *Microstructural Development During Hydration of Cement,* edited by L.J. Struble and P.W. Brown (Mater. Res. Soc. Symp. Proc. **85,** Pittsburgh, PA, 1987), p. 301.
11. T. Knudsen: The dispersion model for hydration of portland-cement 1 general concepts. *Cem. Concr. Res.,* **14,** 622 (1984).
12. T. Knudsen and M. Geiker: Obtaining hydration data by measurement of chemical shrinkage with an archimeter. *Cem. Concr. Res.* **15,** 381 (1985).
13. P.W. Brown, J. Pommersheim, and G. Frohnsdorff: A kinetic-model for the hydration of tricalcium silicate. *Cem. Concr. Res.* **15,** 35 (1985).
14. D.P. Bentz: Three-dimensional computer simulation of Portland cement hydration and microstructure development. *J. Am. Ceram. Soc.* **80,** 3 (1997).
15. D.P. Bentz, E.J. Garboczi, C.J. Haecker, and O.M. Jensen: Effects of cement particle size distribution on performance properties of Portland cement-based materials. *Cem. Concr. Res.* **29,** 1663 (1999).
16. A. Princigallo, P. Lura, K. van Breugel, and G. Levita: Early development of properties in a cement paste: A numerical and experimental study. *Cem. Concr. Res.* **33,** 1013 (2003).
17. L.M. Parrott, M. Geiker, W.A. Gutteridge, and D. Killoh: Monitoring Portland-cement hydration - comparison of methods. *Cem. Concr. Res.* **20,** 919 (1990).
18. G. Papavassiliou, M. Fardis, E. Laganas, A. Leventis, A. Hassanien, F. Milia, A. Papageorgiou, and E. Chaniotakis: Role of the surface morphology in cement gel growth dynamics: A combined nuclear magnetic resonance and atomic force microscopy study. *J. Appl. Phys.* **82,** 449 (1997).
19. J. Greener, H. Peemoeller, C. Choi, R. Holly, E.J. Reardon, C.M. Hansson, and M.M. Pintar: Monitoring of hydration of white cement paste with proton NMR spin-spin relaxation. *J. Am. Ceram. Soc.* **83,** 623 (2000).
20. A.J. Allen, R.C. Oberthur, D. Pearson, P. Schofield, and C.R. Wilding: Development of the fine porosity and gel structure of hydrating cement systems. *Philos. Mag. B* **56,** 263 (1987).
21. J.J. Thomas, H.M. Jennings, and A.J. Allen: The surface area of cement paste as measured by neutron scattering: Evidence for two C-S-H morphologies. *Cem. Concr. Res.* **28,** 897 (1998).
22. J.J. Thomas, H.M. Jennings, and A.J. Allen: The surface area of hardened cement paste as measured by various techniques. *Concr. Sci. Eng.* **1,** 45 (1999).
23. D.R. Vollet and A.F. Craievich: Effects of temperature and of the addition of accelerating and retarding agents on the kinetics of hydration of tricalcium silicate. *J. Phys. Chem. B* **104,** 12143 (2000).
24. D.H.C. Harris, C.G. Windsor, and C.D. Lawrence: Free and bound water in cement pastes. *Mag. Concr. Res.* **26,** 65 (1974).
25. S.A. FitzGerald, D.A. Neumann, J.J. Rush, D.P. Bentz, and R.A. Livingston: In situ quasi-elastic neutron scattering study of the hydration of tricalcium silicate. *Chem. Mater.* **10,** 397 (1998).
26. R. Berliner, M. Popvici, K.W. Herwig, M. Berliner, H.M. Jennings, and J.J. Thomas: Quasielastic neutron scattering study of the effect of water-to-cement ratio on the hydration kinetics of tricalcium silicate. *Cem. Concr. Res.* **28,** 231 (1998).
27. E. Fratini, S-H. Chen, P. Baglioni, and M-C. Bellissent-Funel: Dynamic scaling of quasielastic neutron scattering spectra from interfacial water. *Phys. Rev. E* **64,** 020201 (2001).
28. E. Fratini, A. Faraone, P. Baglioni, M-C. Bellissent-Funel, and

S-H. Chen: Dynamic scaling of QENS spectra of glassy water in aging cement paste. *Physica A* **304,** 1 (2002).
29. E. Fratini, S-H. Chen, P. Baglioni, and M-C. Bellissent-Funel: Quasi-elastic neutron scattering study of translational dynamics of hydration water in tricalcium silicate. *J. Phys. Chem. B* **106,** 158 (2002).
30. S.A. FitzGerald, D.A. Neumann, J.J. Rush, R.J. Kirkpatrick, X. Cong, and R.A. Livingston: Inelastic neutron scattering study of the hydration of tricalcium silicate. *J. Mater. Res.* **14,** 1160 (1999).
31. J.J. Thomas, S.A. FitzGerald, D.A. Neumann, and R.A. Livingston: State of water in hydrating tricalcium silicate and portland cement pastes as measured by quasi-elastic neutron scattering. *J. Am. Ceram. Soc.* **84,** 1811 (2001).
32. S.A. FitzGerald, J.J. Thomas, D.A. Neumann, and R.A. Livingston: A neutron scattering study of the role of diffusion in the hydration of tricalcium silicate. *Cem. Concr. Res.* **32,** 409 (2002).
33. R. Berliner, M. Popovici, K. Herwig, H.M. Jennings, and J. Thomas: High-resolution neutron scattering with commercial thin silicon wafers as focusing monochromators. *Physica B* **241,** 1237 (1997).
34. R.A. Livingston: Fractal nucleation and growth model for the hydration of tricalcium silicate. *Cem. Concr. Res.* **30,** 1853 (2000).
35. J.J. Thomas and H.M. Jennings: Effects of D_2O and mixing on the early hydration kinetics of tricalcium silicate. *Chem. Mater.* **11,** 1907 (1999).
36. A.J. Allen, I.G. Richardson, and G.N. Kearley: (Institute Laue-Langevin: Grenoble, France, 1988) Unpublished results.
37. J.J. Thomas, J. Chen, H.M. Jennings, and A.J. Allen: Effects of decalcification on the microstructure and surface area of cement and tricalcium silicate pastes. *Cem. Concr. Res.* (2004, in press).
38. A.J. Allen, J.J. Thomas, and H.M. Jennings: Composition and density of amorphous calcium–silicate–hydrate gel in cement from combined neutron and x-ray small-angle scattering. *J. Am. Ceram. Soc.,* (2004) (in press).
39. L.F. Brown: LANL Report LA-UR-01-1005 (Los Alamos, NM, 2001).
40. A. Jillavenkatesa, S.J. Dapkunas, and L-S.H. Lum: In *Particle Size Characterization, NIST Special Publication 960-1* (National Institute of Standards and Technology: Gaithersburg, MD, 2001), p. 93.
41. W.K. Brown and K.H. Wohletz: Derivation of the Weibull distribution based on physical principles and its connection to the Rosin-Rammler and lognormal distributions. *J. Appl. Phys.* **78,** 2758 (1995).
42. H.C. Van de Hulst: In *Light Scattering by Small Particles* (John Wiley and Sons, New York, 1962).
43. J.R.D. Copley and T.J. Udovic: Neutron time-of-flight spectroscopy. *J. Res. Natl. Inst. Stand. Technol.* **98,** 71 (1993).
44. J.S. Langer and A.J. Schwartz: Kinetics of nucleation in near-critical fluids. *Phys. Rev. A* **21,** 948 (1980).
45. A.J. Allen, D. Gavillet, and J.R. Weertman: SANS and TEM studies of isothermal M_2C carbide precipitation in ultrahigh strength AF1410 steels. *Acta Metall. Mater.* **41,** 1869 (1993).
46. A.J. Allen and R.A. Livingston: The relationship between differences in silica fume additives and the fine scale microstructural evolution in cement-based materials, *Adv. Cement-Based Mater.* **8,** 118 (1998).